RSC Advances

ROYAL SOCIETY OF CHEMISTRY

www.rsc.org/advances

A series of phosphorus-containing polyimide-POSS nanocomposites were synthesized, phosphorus and POSS synthetic self-passivating layers were formed to protect the underlying material from AO attack.

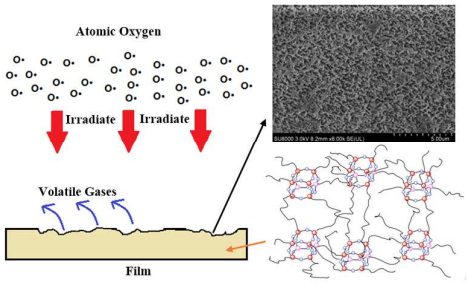

Journal Name

RSCPublishing

ARTICLE

A novel structural polyimide material with phosphorus and POSS synergistic for atomic oxygen resistance

Cite this: DOI: 10.1039/x0xx00000x

Received 00th January 2012,
Accepted 00th January 2012

DOI: 10.1039/x0xx00000x

www.rsc.org/

Guanghe Song [a], Xuesong Li [a], Qiyang Jiang [a], Jianxin Mu* [a] and Zhenhua Jiang [a].

A series of novel structural phosphorus-containing polyimide-polyhedral oligomeric silsesquioxane (POSS) nanocomposites with varying phosphorus contents were synthesized. The nanocomposites displayed outstanding thermal properties. The glass transition temperature was increased to 294.87 °C when the phosphorus content was 1.61 wt% and the anti-degradation properties were also obviously enhanced. Moreover, the nanocomposites presented much higher atomic oxygen (AO) durability compared with pure polyimide because of the incorporation of special functional groups of phosphorus oxide and POSS. The AO erosion yields already decreased to 51.9% of pure polyimide-POSS nanocomposites when the phosphorus content was increased to 1.61 wt%. Furthermore, the mechanism of phosphorus and POSS synergistic AO resistance was explored via XPS and SEM. Three kinds of silicon particles with different binding energies and two kinds of phosphorus elements with different binding energies were formed because of AO exposure and the phosphorus and POSS synergy. Highly effective self-passivating layers were formed to protect the underlying material from AO attack.

Introduction

Most spacecrafts orbit from 200 km–700 km above the earth's surface. At these low Earth orbit (LEO) altitudes, many environmental factors impact the operation and working life of space vehicles. These factors include thermal cycling, microgravity, neutral gas, space debris, UV, radiation and atomic oxygen (AO). AO has been proven to result in serious damage to the external materials of spacecraft in LEO.[1–3] AO is produced by the photodissociation of molecular oxygen in the upper atmosphere. It is a dominant constituent of the remnant atmospheres.[4] The collision between AO and a spacecraft that orbits at the speed of 7 km/s –8 km/s in LEO will generates approximately 5 eV percussive energy on the surfaces of spacecraft.[2] Polyimide has been widely used as a spacecraft material because of its outstanding properties such as high strength, good thermal stability and resistance UV irradiating stability.[5–11] However, AO interacts with polyimide in LEO by complex chemical and physical reactions during constant collisions, the material was eroded and polyimide performance was degraded.[12,13] Thus, developing new high-efficiency techniques to resist AO can prolong working life and enhance the working effectiveness of spacecraft.

The various methods applied for AO resistance could be classified into two categories: one is via the application of protective coatings on the surface of polyimide, the other one is via the introduction of functional compounds into polyimide by physical blend or chemical bond.[14–17] The coatings can also be divided into inorganic, organic and inorganic-organic nanocomposite coatings.[4,18,19] The application of inorganic coating, such as metal and silicone resin coatings, is a standard technique.[20–22] Inorganic coatings are advantageous because of their low erosion yields for AO resistance. Silicone resin coatings produce a SiO_2 layer, which can be called a "self-organized" layer, after AO irradiation. The layer functions as an AO-protective layer and has a self-passivating effect when damaged.[23] However, inorganic coating is so fragile that it is easy to exfoliate, thereby necessitating special care in handling during assembly. Such coating has low reliability to maintain its performance in AO exposure.[15] By contrast, organic coatings possess excellent flexibility and strong adhesion to avoid crack. Furthermore, organic coatings can provide special functions because of their organic functional groups. Nevertheless, they have comparatively higher AO erosion yields than inorganic coatings.[24] Inorganic-organic nanocomposite coatings combine the advantages of both inorganic and organic coatings. However, its application has been restricted due to the phase separation and aggregation in the preparation process.[18,25–27] Given the weakness of protective coatings, several studies mostly have focused on introducing special functional compounds into polyimide to enhance the resistance to AO exposure. For example, polyimides with silicon were quantitatively investigated. Generally, one method is through

blending of polyimide and inorganic SiO_2 via the sol-gel process, the other one is via the copolymerization of polyimide and organic siloxane.[28,29] The advantages of inorganic materials and organic polymers were combined by the polyimide/SiO_2 hybrid. This type of hybird has low AO erosion yields. The process is limited by the aggregation of SiO_2 with increasing SiO_2 content and it also restricts the resistance for AO.[18,30] Polyhedral oligomeric silsesquioxane (POSS), as a siloxane, combines the superior properties of inorganic and organic materials as a result of its unique cage-like molecular structure containing an inorganic silica core surrounded by organic groups.[31,32] The copolymerization of polyimide and POSS to improve the AO durability has already been investigated.[33] Previous studies have indicated that polyimide-POSS nanocomposite materials have outstanding thermal properties and low erosion yields compared with pure polyimides. However, the AO irradiation resistance of these nanomaterials could still be remarkably improved.[23,34] In addition, phosphorus-containing polyimides through phenylphosphine oxide (PPO) group incorporation have attracted much attention. Incorporating PPO groups not only improves the thermal stability of polyimides but also significantly improves the resistance of polyimide to AO irradiation by a self-passivating effect in which a phosphate-enriched surface layer is formed to protect the underlying polyimide from further reaction.[35–38] However, the glass transition temperature (T_g) of phosphorus-containing polyimides hindered their widely application. Thereby the combination of special structure hyperbranched polyimide-POSS system and the excellent AO durable phosphorus-containing polyimide might significantly improved the AO resistance and the thermal properties meanwhile.

In this study, a series of novel structural phosphorus-containing polyimide-POSS nanocomposites were synthesized via solution copolymerization method. Flory gelation theory was applied for the polymerization to avoid gelation. The thermal properties of the nanocomposites were investigated. In addition, the AO exposure experiment was conducted using a ground simulation device and the regularity was confirmed in different AO fluences. Moreover, the chemical compositions and structures, as well as the surface morphologies, before and after AO exposure were also investigated. The results may contribute to provide insight into the synergistic mechanism of phosphorus and POSS for AO resistance.

Experimental

Materials

4, 4'-Diaminodiphenyl ether (ODA) and 3, 3', 4, 4'-biphenyl tetracarboxylic diandhydride (BPDA) were purchased from TCI Shanghai Development Co. Ltd, China. N, N-Dimethylacetamide (DMAC) was obtained from Aladdin Shanghai Development Co. Ltd, China and further purified according to the standard procedures. Octaaminophenyl POSS ($8NH_2$-POSS) was provided by Hybrid Plastics, Inc, USA. Triphenylphosphine oxide (PPO) was also obtained from Aladdin Shanghai Development Co. Ltd, China. Bis (4-aminophenoxy) phenyl phosphine oxide (DAPPO) was synthesized following the previous literature.[39] All the other common reagents were of reagent grade, obtained from commercial source and used as received.

Preparation of phosphorus-containing polyimide-POSS nanocomposite films

The terminal anhydride groups of the phosphorus-containing polyamic acid oligomers were synthesized via copolymerization of ODA, DAPPO and BPDA (Scheme 1). In a three-necked flask equipped with a mechanical stirrer, 50.46 mg of ODA (0.252 mmol) and 33.30 mg of DAPPO (0.108 mmol, 16.01 wt% in the nanocomposites) were added in 20 mL of DMAc and cooled in an ice-water bath in a nitrogen atmosphere. After the diamines were dissolved completely, 117.68 mg (0.400 mmol) BPDA was added and stirred at room temperature for 12 h. A DMAc solution of the terminal anhydride group phosphorus-containing polyamic acid oligomer nanocomposites was obtained. Subsequently, 66.00 mg of $8NH_2$-POSS (5.72×10^{-2} mmol) was added into the phosphorus-containing polyamic acid oligomer solution with continuous stirring at room temperature for 12 h to obtain a DMAc solution of phosphorus-containing polyamic acid-POSS nanocomposites (Scheme 2). The solution was then coated on a glass plate by using an automatic film applicator and heated at 60 °C, 80 °C, 100 °C, 120 °C, 150 °C, 200 °C, 250 °C and 300 °C in a nitrogen atmosphere for thermal imidization. The obtained phosphorus-containing polyimide-POSS nanocomposite film was peeled off from the glass plate and designated as POSS-PI-16P. When the DAPPO contents in the nanocomposites were 0, 11.10 and 22.20 mg (0, 5.55, 10.88 wt%), the corresponding adjustable ODA were 72.08, 64.88 and 57.76 mg, the corresponding relevant adjustable $8NH_2$-POSS were 6.22, 6.34 and 6.48 mg. The corresponding products were named as POSS-PI-0P, POSS-PI-5P and POSS-PI-11P.

Characterization

The Fourier-transform infrared (FTIR) spectrum was recorded using a Nicolet Impact 410 FTIR spectrometer at room temperature (25 °C). Differential scanning calorimetry (DSC) analysis was performed using a Mettler-Toledo Instrument DSC 821e-modulated thermal analyzer at a heating rate of 10 °C/min in a nitrogen purge of 200 mL/min. Thermogravimetric analysis (TGA) was performed using a PerkinElmer Pryis 1 TGA analyzer at a heating rate of 10 °C/min in air purge of 100 mL/min. The surface morphologies of the polyimide films were observed using an SSX-550 Shimadzu scanning electron microscope (SEM). The surface composition and surface chemical states of the polyimide films were measured via X-ray photoelectron spectroscopy by using Escalab 250. AO exposure experiments were conducted using a coaxial source AO ground simulation device and a typical AO flux at the same position (46 cm away from the nozzle) was estimated to be 5.05×10^{15} atoms/cm^2/s. The roughness was evaluated by atomic force microscopy (AFM) using Multimode 8.

Results and discussion

Preparation of phosphorus-containing polyimide-POSS nanocomposites

A series of phosphorus-containing polyimide-POSS nanocomposites were synthesized. Excess BPDA was initially reacted with ODA and DAPPO. Anhydride groups were controlled as the terminal of the phosphorus-containing polyamic acids to facilitate their reaction with $8NH_2$-POSS. However, this reaction is a typical A_2+B_8 reaction, whereby polyamic acid is A_2 and $8NH_2$-POSS is B_8. Gelation easily occurs if the ratio is located in the gelation scope according to the Flory gelation theory.[40–42] Thus, the key to copolymerization is to establish a suitable ratio of the terminal anhydride of the polyamic acid to the amine group of the POSS. Calculated and experimental results show that the ratio was 7:1. The network-structured phosphorus-containing polyamic acid-POSS nanocomposites were synthesized. To obtain excellent phosphorus-containing polyimide-POSS nanocomposites films, the controllability of temperature programming was essential. The mass percentages of the phosphorus and $8NH_2$-POSS in the nanocomposites are displayed in Table 1.

Polymer characterization

The FTIR spectra of the nanocomposites are shown in Fig. 1. In the polyimides, a sharp and strong peak attributed to the Si-O-Si stretching of the silsesquioxane cage appeared at 1100 cm^{-1}. The characteristic imide group bands at 1770, 1710 and 1380 cm^{-1} completely disappeared, which implied a fully imidized structure. The polyimide-derived C=C aromatic ring absorption at 1500 cm^{-1} was observed. Aromatic ether C-O-C stretching vibration was found at 1245 cm^{-1}. Ph-P appeared at 1420 cm^{-1}. The peak became stronger with increasing phosphorus content, which confirmed that a phosphonate structure exists in POSS-PI-5P, POSS-PI-11P and POSS-PI-16P.

Thermal properties of polymer

The polyimides were subjected to DSC to measure their T_g values and the DSC curves are shown in Fig. 2. The T_g values are displayed in Table 1. The T_g values of the polyimides increased with the phosphorus content in the polyimide. Pure polyimide-POSS nanocomposite exhibited high T_g value because of the nanoreinforcement of the POSS cages within the polyimide nanocomposite network. However, the phosphorus-containing polyimide-POSS nanocomposites have higher T_g values than pure polyimide-POSS. With the introduction of DAPPO in the main chain of polyimides, the C electron cloud density and intermolecular forces increased because of the P=O bond, which provided the electronic properties that resulted in the difficulty of segmental motion and increased T_g. The thermal stability of the polyimide-POSS nanocomposite materials were evaluated via TGA and Fig. 3 presents the TGA thermograms in atmosphere. An evident increase in both 5% T_d and 10% T_d was observed for the phosphorus-containing polyimide-POSS nanocomposites compared with the pure polyimide-POSS nanocomposites. This phenomenon was due to the P=O with high bond energy, which resulted in higher degradation temperature of DAPPO than ODA. However, almost no difference was found in the decomposition temperatures of phosphorus-containing polyimide-POSS nanocomposites because of their similar structures. The phosphorus-containing polyimide-POSS nanocomposites displayed significantly higher residuals of degradation than pure polyimide-POSS nanocomposites and the char yieldss of these polyimides increased with phosphorus content. The increased yields of degradation residues were ascribed to the introduction of DAPPO in the polyimide main chain during thermal decomposition. The values of T_g, 5% T_d, 10% T_d and char yields of these polyimide nanocomposites are shown in Table 1.

AO exposure results

The AO irradiation tests were essential to investigate the performance of polyimide-POSS nanocomposite films for AO resistance. All polyimide films were tested using a coaxial source AO ground simulation device. To evaluate the AO fluence on the films, mass measurement and surface qualitative analysis were performed before and after AO irradiation. The erosion yields of the polyimide-POSS nanocomposite films can be determined by the following equation: [22]

$$E = \Delta M/\rho \times A \times F$$

where E is the erosion yields (cm^3/atoms), ΔM is the mass loss (g), A is the surface area of the sample (cm^2), ρ is the density (g/cm^3) and F is the total AO fluence (atoms/cm^2). When the tested time is 12h, F is 2.27×10^{20} atoms/cm^2. So the tested time extended to 24h, corresponding F is 4.53×10^{20} atoms/cm^2. Table 2 shows the mass loss in the exposure of total AO fluences of 2.27×10^{20} and 4.53×10^{20} atoms/cm^2. The corresponding calculated erosion yields are also displayed in Table 2. The AO resistance of phosphorus-containing polyimide-POSS film was one order of magnitude lower than that of Kapton which is the pristine polyimide ($E=3.0\times10^{-24}$ cm^3/ atoms).[43] Although the pure polyimide-POSS nanocomposites showed a low erosion yields, the phosphorus-containing polyimide-POSS nanocomposites films presented significantly lower erosion yields (Fig. 4). After exposure to total AO fluence of 2.27×10^{20} atoms/cm^2, the erosion yields of POSS-PI-5P, with a phosphorus mass content of 0.56 %, decreased sharply to 68.7% of the pure polyimide-POSS nanocomposites. Furthermore, the erosion yields of POSS-PI-16P decreased to only 51.9% of pure polyimide-POSS nanocomposites when the mass content of phosphorus was increased to 1.61 %. The same tendency was found for the polyimide-POSS nanocomposite films after exposure to higher total AO fluence of 4.53×10^{20} atoms/cm^2. These results revealed the enhanced AO durability of phosphorus-containing polyimide-POSS nanocomposites films compared with the pure polyimide-POSS nanocomposite films. The AO durability of phosphorus-containing polyimide-POSS nanocomposite films increased with phosphorus content, which indicated that the introduction of phosphorus oxides could decrease the AO erosion yields.

Surface compositional and structural change

The surface compositions of the pure polyimide-POSS nanocomposite films (POSS-PI-0P) and the phosphorus-containing polyimide-POSS nanocomposite films (POSS-PI-16P) before and

after AO exposure to 2.27×10^{20} atoms/cm^2 of AO fluence obtained from XPS data are summarized in Table 3. Given the AO exposure for the pure polyimide-POSS nanocomposite films, the concentration of the irradiated-surface nitrogen atoms, which belong to amide bond, dramatically decreased to almost half compared with that of pristine nanocomposite. Carbon concentration also decreased. This phenomenon was due to the reaction of nitrogen and carbon on the surface with oxygen atoms to form a volatile gas that released to the environment. However, silicon and oxygen concentrations increased. The increasing silicon atoms concentrate was due to the decreasing concentrations of the other atoms caused by the stability of silicon as inorganic element. High-resolution XPS spectra exhibited that the Si 2p peak position derived from the pristine surface location at 102.0 eV corresponded to the O-Si-O ($SiO_{3/2}$) in the POSS cages (Fig. 5a).[40] However, the Si 2p peak derived from the irradiated surface after AO exposure was divided into three different shifts located at 102.0, 103.0 and 104.6 eV. The binding energy of 102.0 eV was still existent indicated that the O-Si-O bonds of POSS did not disappear. But the occurrence of two new binding energies revealed the formation of new structures. This phenomenon demonstrated that the regular POSS cages were damaged to imperfection rather than be fully destroyed because the binding energy of Si 2p obtained from the pristine surface remained. In addition, the three different chemical environments of silicon most likely existed as (a) $SiO_{3/2}$, which belongs to POSS, (b) SiO_2 and (c) O=Si-O (Fig. 5d) according to the binding energy, regardless of the structural situations of the imperfect cages.[18,19,44] These observations also indicated that the increasing oxygen concentration was due to the reaction of a portion of silicon with oxygen to form new silicon oxides with higher oxygen content.

Similarly, the irradiated-surface carbon concentration of POSS-PI-16P decreased compared with the pristine nanocomposite because the carbon reacted with oxygen to form volatile gas, which released to the environment because of AO exposure. The nitrogen concentration derived from the XPS data almost remained unchangeable. It demonstrated that the phosphorus-containing polyimide-POSS nanocomposites displayed better AO resistance. In addition, the silicon, oxygen and phosphorus concentrations increased. The increasing silicon concentrations and phosphorus concentrations was due to the reduction in the concentrations of the other atoms caused by the stability of silicon and phosphorus as inorganic elements. The XPS spectra in Fig. 5b exhibited that the Si 2p assigned to a binding energy of 102.0 eV from the pristine surface corresponding to $SiO_{3/2}$, which belongs to the POSS cages. After AO exposure, three peaks appeared in the Si 2p region with binding energies of 102.0, 103.2 and 104.5 eV, which indicated that the formation of two new silicon oxides and the regular POSS cages were damaged to imperfect structures primarily caused by the same reason as that of the pure polyimide-POSS nanocomposites. The three different silicon particles also most likely correspond to $SiO_{3/2}$, SiO_2 and O=Si-O (Fig. 5d). The P 2p peaks obtained from the pristine nanocomposite and AO-irradiated surface of POSS-PI-16P were also compared as shown in Fig. 5c. The binding energy of P 2p corresponding to the DAPPO located at 132.1 eV from the pristine surface. After AO exposure, the two new peaks of P 2p located at 132.9 and 134.1 eV belonged to phosphate and metaphosphate on the irradiated surface.[45,46] The increasing oxygen concentration was reasonable because of the formation of silicon oxides, phosphate and metaphosphate with higher oxygen content. These observations showed that the irradiated surface of phosphorus-containing polyimide-POSS nanocomposite films produced a layer which consisted of imperfect POSS, silicon oxides, phosphate and metaphosphate. The layer covered on the irradiated surface and protected the underlying material from AO attacking due to the stability of inorganics. It caused the enhancement for AO resistance of the phosphorus-containing polyimide-POSS nanocomposites films. Furthermore, the AO erosion yields decreased when the AO exposure time extended to double with the higher total AO fluence of 4.53×10^{20} atoms/cm^2, the working of the passivating layer has been examined again.

Surface morphology

Prior to AO exposure, the pristine polyimide-POSS nanocomposites films were transparent with light yellow colors and smooth surfaces. After AO exposure, the surface of polyimide-POSS nanocomposites films was roughened significantly because of volatilization caused by the formation of volatile oxides. The surface morphology of a series polyimide-POSS nanocomposite films after AO exposure for 2.27×10^{20} atoms/cm^2 were photographed via SEM and the surface roughness were explored by AFM. The roughness caused by the AO erosion. The surface roughness decreased remarkably with increasing phosphorus content according to the photographs of Fig. 6 and the data in Table 2. The surface of pure polyimide-POSS nanocomposite films was roughest, which indicated it suffered the most serious erosion. The pure polyimide-POSS nanocomposite films produced a passivating layer, which consisted of imperfect POSS and silicon oxides that could protect the polyimide from attacking of AO, but they were too sparsely scattered on the surface of the film to function effectively. The roughness decreased with the introduction of phosphorus. Because the phosphorus-containing polyimide-POSS nanocomposites produced not only imperfect POSS and silicon oxides layer but also phosphate and metaphosphate layer. Additionally, they presented a more homogeneous distribution because of the formation of phosphate and metaphosphate layer located at the positions that belonged to the polyimide chain. So they filled the blanks that could not be covered by the layer of imperfect POSS and silicon oxides. The passivating layer of phosphorus-containing polyimide-POSS nanocomposite films was evidently thicker compared with the pure one. It demonstrated the introduction of phosphorus into the polyimide-POSS system can improve the AO durability. Unlike the SiO_2 coating or phosphate coating applied to the surface, the formation of imperfect POSS and silicon oxides layer, as well as the phosphate and metaphosphate layer, exhibited self-passivating and restored function. These layers could react with incident AO to create more phosphate, metaphosphate, imperfect POSS and silicon oxides if the defects developed. Moreover, the imperfect POSS would also react with AO to form new silicon oxides during AO attack. However, the formation of phosphate and metaphosphate layers increased with increasing phosphorus content of the phosphorus-containing

polyimide-POSS. Thus, the surface morphology became flatter and the roughness decreased with increasing phosphorus content. In addition, the thick formation distribution of imperfect POSS, silicon oxides, phosphate and metaphosphate layer collaboratively protected the films from AO attack. Hence, the polyimide-POSS nanocomposites film with the highest phosphorous content has the best AO resistance.

Conclusions

In this article, a series of novel structural phosphorus-containing polyimide-POSS nanocomposites, which incorporated phosphorus and POSS into the main chain of polyimide, were successfully synthesized. The structures of these phosphorus-containing polyimide-POSS nanocomposites were characterized via FTIR spectroscopy. The DSC data showed that the T_g of the POSS-polyimide nanocomposites films increased significantly with increasing phosphorus content. The TGA data indicated that the stability of the phosphorus-containing polyimide-POSS nanocomposites was markedly improved in terms of temperatures at the maximum rate of degradation and the yields of degradation residues. Given the presence of phosphorus-containing monomer DAPPOs in the phosphorus-containing polyimide-POSS hybrid films, the AO erosion yields of these films were remarkably lower than those of the pure polyimide-POSS hybrid films. Meanwhile, the surface roughness of phosphorus-containing polyimide-POSS decreased obviously compared with that of the pure polyimide-POSS hybrid film after AO fluence of 2.27×10^{20} atoms/cm^2. Moreover, XPS data showed the variation in both chemical composition and chemical binding energy before and after AO exposure. The results indicated that the passivating phosphate and metaphosphate surface layer had been formed on the film surface after AO exposure caused by the introduction of phosphorus-containing monomer DAPPO into the nanocomposites. The phosphate and metaphosphate surface layers filled the blank, which did not cover by the imperfect POSS and silicon oxide layer. The thick passivating layers protected the film from AO erosion collaborative synergistically. Therefore, the phosphorus-containing polyimide-POSS hybrid films displayed excellent AO erosion resistance.

Acknowledgements

The authors gratefully acknowledge the financial support from the International Science and Technology Cooperation program of China (2012DFR50300).

Notes and references

[a] College of Chemistry, The Key Lab of High Performance Plastics, Ministry of Education, Jilin University, ChangChun 130012, China.

† Footnotes should appear here. These might include comments relevant to but not central to the matter under discussion, limited experimental and spectral data, and crystallographic data.

Electronic Supplementary Information (ESI) available: [details of any supplementary information available should be included here]. See DOI: 10.1039/b000000x/

1 P. Pattabiraman, N. M. Rodriguez, B. Z. Jang and R. T. K. Baker, Carbon, 1990, **28**, 867-878.
2 A. Rahnamoun and A. C. T. van Duin, J Phys Chem A, 2014, **118**, 2780-2787.
3 A. R. Chambers, I. L. Harris and G. T. Roberts, Mater Lett, 1996, **26**, 121-131.
4 S. Packirisamy, D. Schwam and M. H. Litt, J Mater Sci., 1995, **30**, 308-320.
5 Tung-Lin Li and Steve Lien-Chung Hsu, J. Mater. Chem., 2010, **20**, 1964-1969.
6 Anindita Ghosh, Suman Kumar Sen, Susanta Banerjee and Brigitte Voit, RSC Adv., 2012, **2**, 5900-5926.
7 Shigetoshi Matsui, Hiroki Sato and Tsutomu Nakagawa, J Membrane Sci., 1998, **141**, 31-43.
8 Der-Jang Liaw, Feng-Chyuan Chang, Man-kit Leung, Meng-Yen Chou and Klaus Muellen, Macromolecules, 2005, **38**, 4024-4029.
9 Po Jen Wang, Ching Hsuan Lin, Sheng Lung Chang and Shao-Ju Shih, Polym. Chem., 2012, **3**, 2867-2874.
10 Guofeng Tian, Shengli Qi, Fei Chen, Lei Shi, Wenping Hu and Dezhen Wu, Applied Physics Letters, 2011, **98,** 203302.
11 Deyang Ji, Lang Jiang, Xiaozhou Cai, Huanli Dong, Qing Meng, Guofeng Tian, Dezhen Wu, Jingze Li and Wenping Hu, Organic Electronics, 2013, **14**, 2528-2533.
12 Suman Kumar Sena and Susanta Banerjee, RSC Adv., 2012, **2**, 6274-6289.
13 Timothy K. Minton, Michael E. Wright, Sandra J. Tomczak, Sara A. Marquez, Linhan Shen, Amy L. Brunsvold, Russell Cooper, Jianming Zhang, Vandana Vij, Andrew J. Guenthner and Brian J. Petteys, ACS Appl Mater Inter, 2012, **4**, 492-502.
14 Verker R, Grossman E, Gouzman I and Noam Eliaz, Polymer, 2007, **48**, 19-24.
15 Hiroyuki Shimamura and Takashi Nakamura, Polym Degrad Stabil, 2009, **94**, 1389–1396.
16 Jeffreyw. Gilman, David S. Schlitzer and Josephd. Lichtenhan, J Appl Polym Sci., 1996, **60**, 591-596.
17 M. Raja Reddy, N. Srinivasamurthy and B. L. Agrawal, Surf Coat Tech, 1993, **58**, 1–17.
18 Shuwang Duo, Meishuan Li, Ming Zhu and Yanchun Zhou, Surf Coat Tech, 2006, **200**, 6671–6677.
19 Shuwang Duo, Meishuan Lia, Ming Zhua and Yanchun Zhoua, Mater Chem Phys, 2008, **112**, 1093–1098.
20 Bruce A. Banks, Aaron Snyder, Sharon K. Miller, Kimk. De Groh and Rikako Demk, J Spacecraft Rockets, 2004, **41**, 335-339.
21 Russell Cooper, Hari P. Upadhyaya, Timothy K. Minton, Michael R. Berman, Xiaohua Du and Steven M. George, Thin Solid Films, 2008, **516**, 4036–4039.
22 Irina Gouzman, Olga Girshevitz, Eitan Grossman, Noam Eliaz and Chaim N. Sukenik, Appl. Mater. Interfaces, 2010, **2**, 1835–1843.

23 Deepa Devapal, S. Packirisamy, Raji M. Korulla and K. N. Ninan, J Appl Polym Sci., 2004, **94**, 2368–2375.
24 Longfei Hu, Meishuan Li, Caihong Xu, Yongming Luo and Yanchun Zhou, Surf Coat Tech, 2009, **203**, 3338–3343.
25 Fei Xiao, Kai Wang and Maosheng Zhan, Appl Surf Sci., 2010, **256**, 7384–7388.
26 XinZhang, LeiMao, JunDu and HuiJunWei, J Sol-gel Sci Techn, 2014, **69**, 498–503.
27 Analia I. Romero, Mo´nica L. Parentis, Alberto C. Habert and Elio E. Gonzo, J Mater Sci., 2011, **46**, 4701-4709.
28 Lili Zhang, Guofeng Tian, Xiaodong Wang, Shengli Qi, Zhanpeng Wu and Dezhen Wu, Compos Part B-Eng, 2014, **56**, 808–814.
29 Xing F. Lei , Ying Chen , He P. Zhang , Xiang J. Li , Pan Yao and Qiu Y. Zhang, Appl. Mater. Interfaces, 2013, **5**, 10207–10220.
30 C. Xenopoulos, L. Mascia and S. J. Shaw, J. Mater. Chem., 2002, **12**, 213-218.
31 Kazuo Tanaka and Yoshiki Chujo, J. Mater. Chem., 2012, **22**, 1733-1746.
32 Chyi-Ming Leu, G. Mahesh Reddy, Kung-Hwa Wei and Ching-Fong Shu, Chem. Mater, 2003, **15**, 2261-2265.
33 Shawn H. Phillips, Timothy S. Haddad and Sandra J. Tomczak, Curr Opin Solid ST M, 2004, **8**, 21-29.
34 A.L. Brunsvold, T.K. Minton, I. Gouzman, E. Grossman and R. Gonzalez, High Perform. Polym, 2004, **16**, 303–318.
35 Kent A. Watson, Frank L. Palmieri and John W. Connell, Macromolecules, 2002, **35**, 4968-4974.
36 Fei Xiao, Kai Wang and Mao Sheng Zhan, J Mater Sci., 2012, **47**, 4904–4913.
37 J. W. Connell, J. G. Smith Jrt and P. M. Hergenrother, Polymer, 1995, **36**, 5-11.
38 J.G Smith Jr, J.W Connell and P.M Hergenrother, Polymer, 1994, **35**, 2834–2839.
39 Ying-Ling Liu, Ging-Ho Hsiue, Rong-Ho Lee and Yie-Shun Chiu, J Appl Polym Sci., 1997, **63**, 895–901.
40 Walter H. Stockmayer, J. Chem. Phys., 1943, **11**, 45-55.
41 Walter H. Stockmayer and Edward F. Casassa, J. Chem. Phys., 1952, **20**, 1560-1566.
42 Nita Xu, Edmund J. Stark, Petar R. Dvornic, Dale J. Meier, Jin Hu and Claire Hartmann-Thompson, Macromolecules**,** 2012, **45**, 4730–4739.
43 Yuanyuan Xie, Yuan Gao, Xiaogang Qin, Huitao Liu and Jungang Yin, Surf Coat Tech, 2012, **206,** 4384-4388.
44 Shuwang Duo, Huan Ke, Tingzhi Liu, Mimi Song and Meishuan Li, Nucl Instrum Meth B, 2013, **307**, 324-327.
45 Barbaux Y, Dekiouk M, Le Maguer D, Gengembre L, Huchette D and Grimblot J, Appl Catal A-GEN, 1992, **90**, 51-60.
46 Ping Ho Lo, Wen Ta Tsai, Ju Tung Lee and Ming Pan Hung, J Electrochem SOC, 1995, **142**, 91-96.

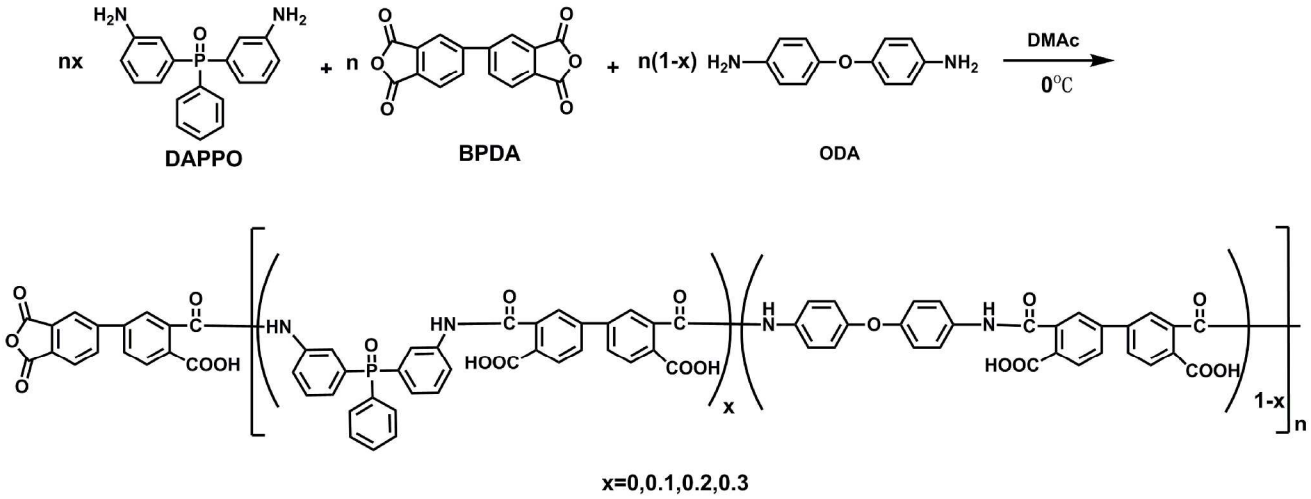

Scheme 1 Synthesis of the anhydride groups as terminal of the phosphorus-containing polyamic acid oligomers.

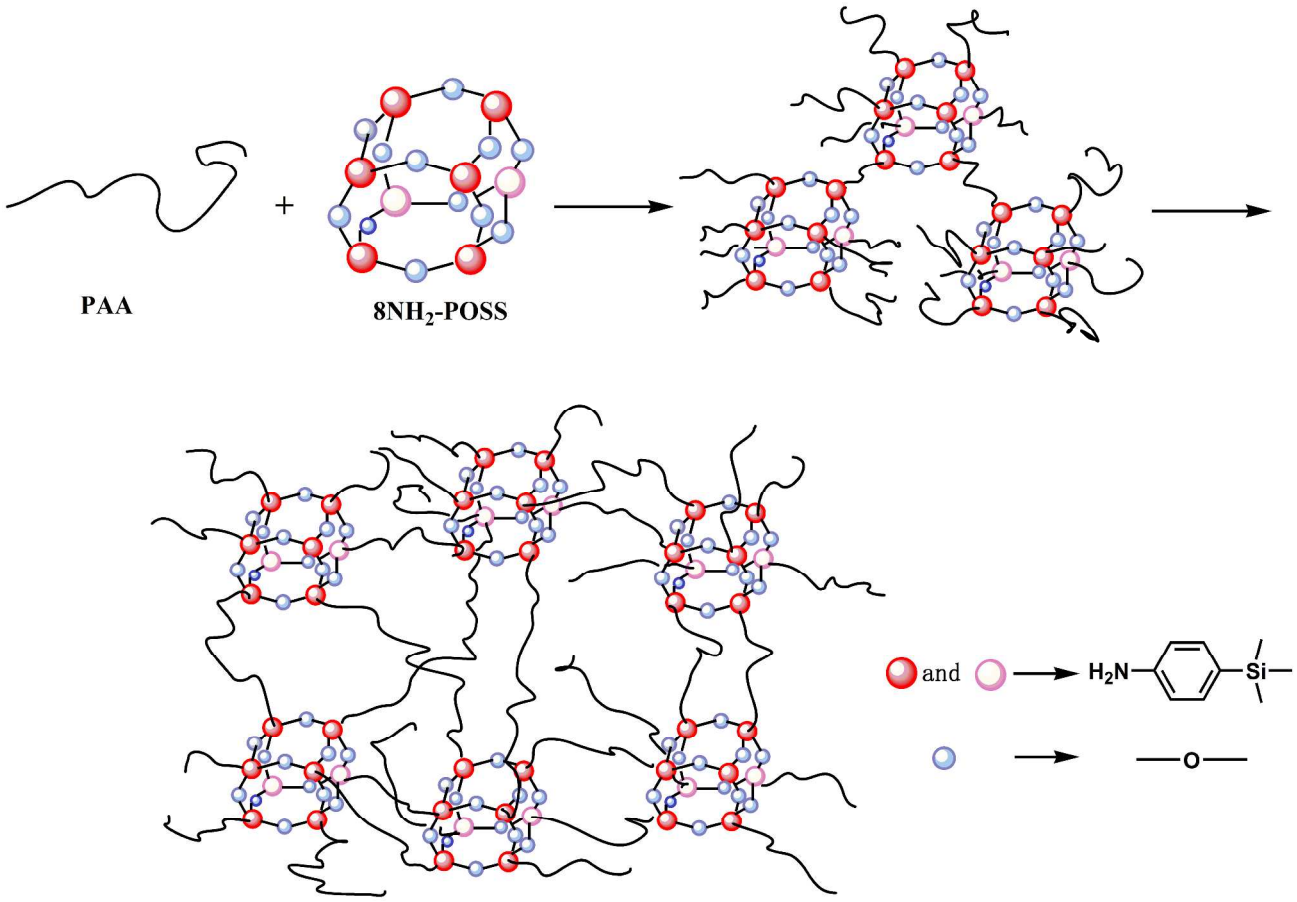

Scheme 2 Synthesis of phosphorus-containing polyamic acid-POSS nanocomposites.

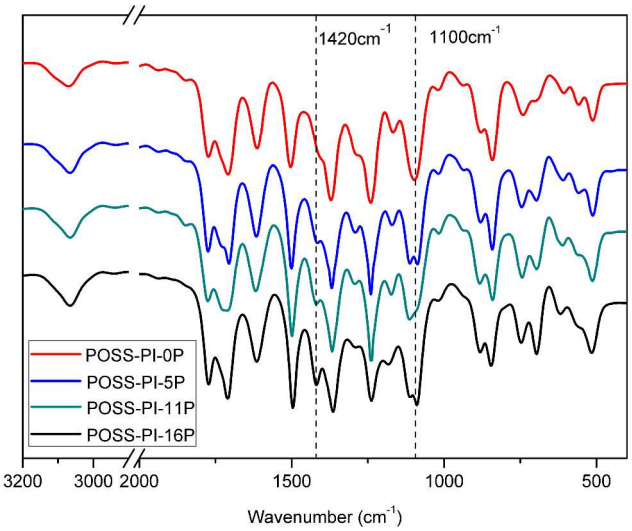

Fig. 1 FT-IR spectra of POSS-PI-0P, POSS-PI-5P, POSS-PI-11P and POSS-PI-16P.

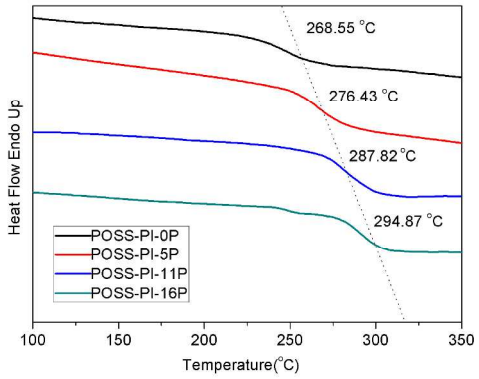

Fig. 2 DSC curves of POSS-PI-0P, POSS-PI-5P, POSS-PI-11P and POSS-PI-16P.

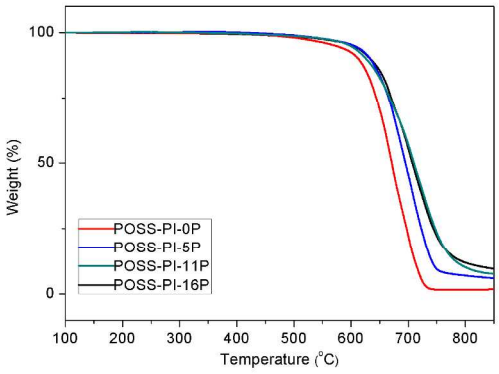

Fig. 3 TGA curves of POSS-PI-0P, POSS-PI-5P, POSS-PI-11P and POSS-PI-16P.

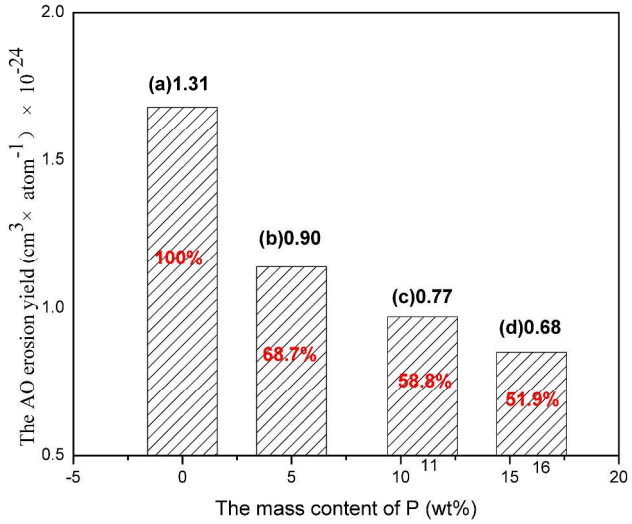

Fig. 4 The AO erosion yields of (a) POSS-PI-0P, (b) POSS-PI-5P, (c) POSS-PI-11P and (d) POSS-PI-16P irradiated by the total AO fluence of 2.27×10^{20} atoms/cm^2.

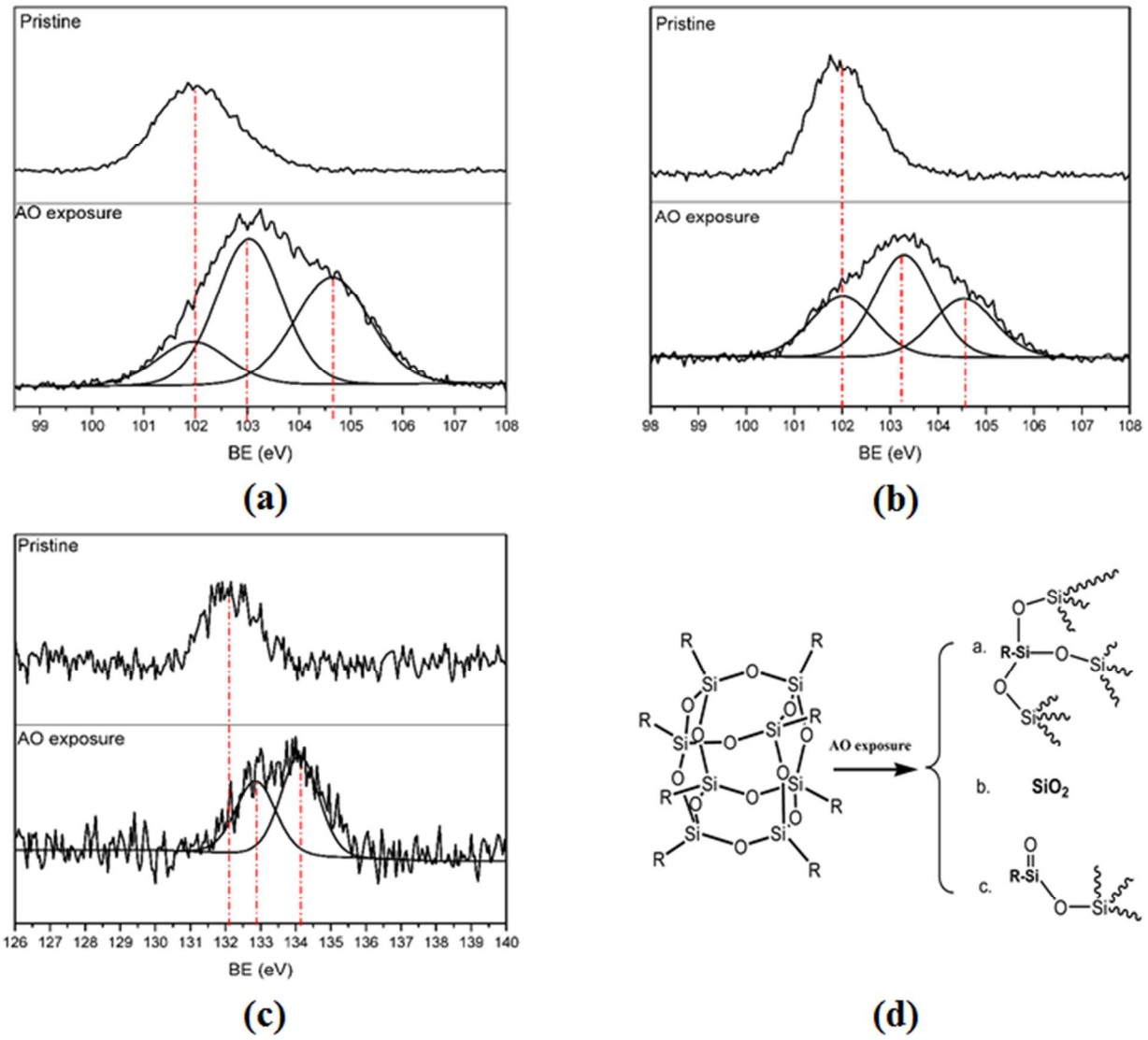

Fig. 5 XPS data of Si 2p spectra of (a) POSS-PI-0P and (b) POSS-PI-16P; P 2p spectra of (c) POSS-PI-16P; (d) the structures of three different BE of Si 2p.

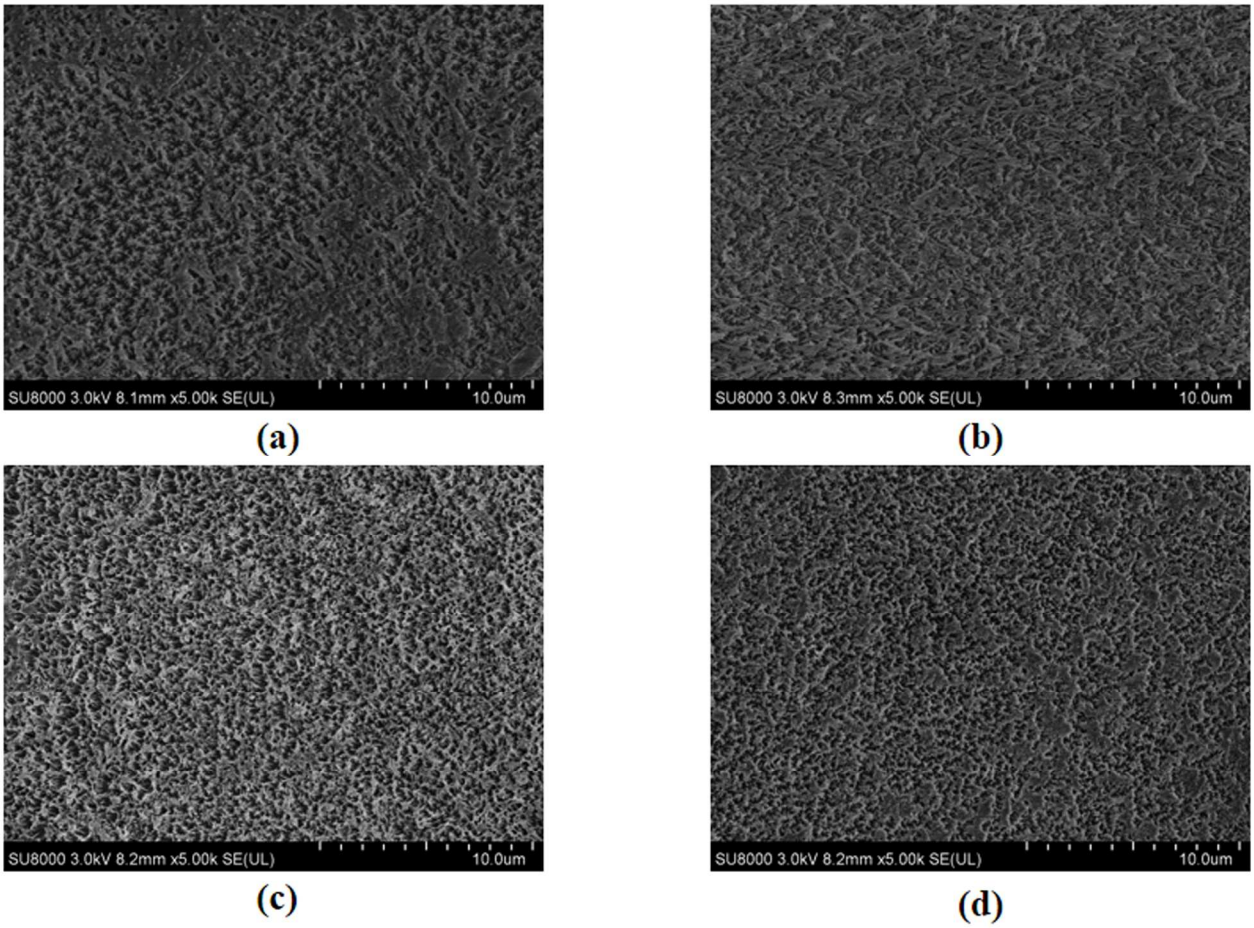

Fig. 6 SEM photographs of (a) POSS-PI-0P, (b) POSS-PI-5P, (c) POSS-PI-11P and (d) POSS-PI-16P hybrid films after AO exposure.

Table 1 Summary of Properties of POSS-PI-0P, POSS-PI-5P, POSS-PI-11P and POSS-PI-16P

Samples	T_g (°C)[a]	5%T_d (°C)[b]	10%T_d (°C)[c]	Residue by Weight (%)[d]	POSS (wt%)[e]	P (wt%)[f]
POSS-PI-0P	268.55	572.43	612.8	1.641	3.1725	0
POSS-PI-5P	276.43	605.25	633.57	6.925	3.1725	0.56
POSS-PI-11P	288.32	598.27	626.07	10.124	3.1725	1.09
POSS-PI-16P	294.87	602.45	633.58	11.873	3.1725	1.61

a DSC at a heating rate of 10 °C min^{-1} in nitrogen
b Temperature at which 5% weight loss was recorded by TGA at a heating rate of 10 °C min^{-1} in air.
c Temperature at which 10% weight loss was recorded by TGA at a heating rate of 10 °C min^{-1} in air.
d The yields of degradation residues were taken as the values at 800 °C in air.
e The mass fraction of POSS in the hybrid system.
f The mass fraction of phosphorus in the hybrid system.

Table 2 Summary of the mass loss， AO erosion yields and roughness.

Samples	F=2.27×10^{20} atoms/cm^2		F=4.53×10^{20} atoms/cm^2		R_q (nm)[e]
	ΔM (g)[a]	E×10^{24} (atoms /cm^3)[b]	ΔM (g)[c]	E×10^{24} (atoms /cm^3)[d]	
POSS-PI-0P	1.68	1.306	2.43	0.9438	167
POSS-PI-5P	1.14	0.9047	2	0.7936	141
POSS-PI-11P	0.97	0.7753	1.65	0.6594	136
POSS-PI-16P	0.85	0.6844	1.41	0.5676	132

a The mass loss of polyimides in the AO fluence of 2.27×10^{20} atoms/cm^2.

b The AO erosion yields of the polyimides in the AO fluence of 2.27×10^{20} atoms/cm^2.
c The mass loss of polyimides in the AO fluence of 4.53×10^{20} atoms/cm^2.
d The AO erosion yields of the polyimides in the AO fluence of 4.53×10^{20} atoms/cm^2.
e The root-mean-square roughness values of the polyimide surfaces which irradiated by total AO fluence of 2.27×10^{20} atoms/cm^2.

Table 3 Surface atomic concentration (in percent) determined from XPS survey scans

Sample		Concentration (%)				
		C1s	O1s	N1s	Si2p	P2p
POSS-PI-0P	Virgin	73.64	27.74	4.11	12.91	---
	AO exposure	57.18	15.57	2.18	6.68	---
POSS-PI-16P	Virgin	75.59	17.15	2.82	3.91	0.53
	AO exposure	70.18	18.45	2.89	7.59	0.89